Progress In Electromagnetics Research, PIER 16, 227–267, 1997

COMPARISON BETWEEN THE PERFORMANCE OF Ti:$LiNbO_3$ AND H:$LiNbO_3$ ROTATED OPTICAL AXIS WAVEGUIDES

F. Prudenzano, A. D'Orazio, V. Petruzzelli, and M. De Sario

Dipartimento di Elettrotecnica ed Elettronica
Politecnico di Bari
Via E. Orabona 4 - 70125 Bari, Italy

1. INTRODUCTION

The first lithium niobate boule was synthesized and investigated several years ago at Bell Laboratories, as documented in a series of papers published in 1966, however the first metal diffused optical waveguide in lithium niobate (Me:$LiNbO_3$) was fabricated in 1974. Since then, over the last two decades, integrated optics researchers have widely investigated and exploited this material as an ideal substrate of waveguiding structures [1–11]. The $LiNbO_3$ technology was rapidly used in more fields of applied research, allowing the construction of many high performance passive and semi-active devices. In fact, $LiNbO_3$ has a great number of physical properties (elastooptical, electrooptical, piezoelec-

trical, pyroelectrical etc.) which are employed in the fabrication of modulators, sensors, directional couplers, spectrum analyzers, filters, polarization converters, switches, and so on. The first successful applications in the nonlinear optics [2] and laser emission [3] have produced a new growing interest for this excellent material and have reencouraged the theoretical analysis of electromagnetic propagation in typical Ti:$LiNbO_3$ and H:$LiNbO_3$ waveguiding structures [4–10].

$LiNbO_3$ device research has led to a more accurate understanding of Ti indiffusion technology and to the development of other fabrication processes, such as proton-exchange and ion implantation. Ti:$LiNbO_3$ technology allows the simple fabrication of low-loss reliable and highly stable waveguides. Moreover, it does not compromise the electrooptic crystal properties. Proton exchange H:$LiNbO_3$, on the other hand, permits higher surface refractive index changes with a simpler fabrication process, but the strength of the electrooptic effect and the waveguide stability can be maintained only by using particular procedures and stratagems (e.g. post-annealing).

Fortunately, new solutions are continuously proposed in the field of $LiNbO_3$ technology and its application. As an example, in a recent work, the quality of annealed proton-exchange and graded proton-exchange in domain-inverted $LiNbO_3$ samples was discussed [5]. The graded proton exchanged waveguides are well suited to the field of quasi-phase-matching non-linear components and to the fabrication of waveguide devices based on spatial manipulation of the non-linear, electrooptic and piezoelectric coefficients in lithium niobate. Moreover, this technique has been proposed to simplify sophisticated electrode patterns by using the change sign of the electrooptic coefficient through domain inversion, i.e. in building high frequency modulators. Recent applications to sensors and narrowband mode converters employ combined Ti-diffused and proton-exchanged waveguiding structures [6].

Other interesting applications of planar multimode $LiNbO_3$ waveguides regard the parametric intermode scattering [7]. In fact, light causes a refractive index change in planar lithium niobate waveguides, via the photorefractive effect. This phenomenon can also be obtained in waveguiding structures having small thickness, for which gratings can be recorded even when the photovoltaic or diffusion current is orthogonal to the wave vector. On the other hand, the interference of the incident beam and the scattered waves can write gratings in the material through the optical Kerr effect. So various four-wave mixings

are possible and, in particular, two beam holographic recording and phase conjugation in backward four wave mixing. Phase conjugation, in a multimode waveguiding structure, can involve both guided and leaky modes. Recently, both pump and scattered waves having leaky behaviour have been observed in third order interactions, in both X and Y-cut $LiNbO_3$:Ti:Fe waveguides, where the iron diffusion allows the enhancement of the photorefractive effect [7].

Leaky propagation phenomenon has been exploited to fabricate several microwave devices. The bandwidth of electro-absorption modulators, for millimeter-wave application, can be enhanced by using distributed coupling of leaky waves.

These kinds of surface modes can also be applied within the field of integrated optics. In fact, research interest towards leaky propagation in $LiNbO_3$ waveguides started a few years ago. As an example, an optical switching device employed the strong peak of the decay constant near the propagation direction in which the leaky modes convert to guided waves. The transition from leaky to guided waves was attained electrooptically and the most suitable optical c-axis orientation was chosen [8]. Therefore, the knowledge of guided and leaky mode dispersion in anisotropic waveguides is fundamental in order to refine and optimize such optical devices. On the other hand, the leaky modes can appear as noise in guided mode excitation by means of end-firing technique, so their nature and behaviour must be well stated in every waveguiding structure in which they could be supported. The leaky waves, characterized by having co-leaky nature with an outcoming power flow from the core to the open media, have been well identified in the field of microwave antennas, millimeter-wave and guided optics configurations. These waves are not considered in this work. On the contrary, two other kinds of leaky waves are treated. The former are the contra-leaky waves which leak into the substrate and have an incoming power flow to the core from air. These waves may be excited in our waveguiding structure, for example, by means of prism configuration or end firing arrangement. The latter are the co-leaky waves, having a power flow incoming to the core from both the substrate and the air. They correspond to surface waves supported by a lossy layer in which the incoming power flow compensates for the power loss, and they cover the guided mode propagation case.

So a general computer code procedure, which allows the analysis of both kinds of excitable leaky waves and guided propagation, for every

dielectric tensor configuration, has been implemented. The reliability of the computer code is accurately tested.

The waveguiding structures treated in the following investigation are typically employed in electrooptic Ti:$LiNbO_3$ devices [9]. These require the construction of suitable five-layered structures. In fact, for the Y-cut configuration, an overlay is located on the electrode in order to bound the electromagnetic field under the metal region to enhance the coupling of light with the modulating signal [9]. Therefore, in previous papers [4,10], the guided and leaky modes supported by a Ti:$LiNbO_3$ planar five-layered waveguide having both longitudinal and polar dielectric tensor configurations have been analyzed.

The simulation analysis of Ti:$LiNbO_3$ waveguides is completed in this work, by examining the behaviour of the multilayered structure having the equatorial dielectric tensor configuration. In this dielectric tensor configuration, the optical c-axis lies in the transverse-lateral xz plane. The structure supports pure TM and TE polarized waves; i.e. there are no hybrid solutions of the Maxwell equations. The pure TE mode propagation is not investigated because it depends only on the extraordinary refractive index and is similar to that supported by isotropic waveguides. On the contrary, the TM mode characteristics depend on both extraordinary and ordinary indices and have complex refractive effective indices and amplitude coefficients. So, in the following, the dependence of the TM wave modal properties on the angle γ between the optical c-axis and the coordinate z axis will be determined. The effects of the presence of four different metal layers (gold, silver, aluminium and nickel) and of the variation of the refractive index of the overlay (a composition of SiO_2-Ta_5O_5) on the complex refractive effective index will be outlined.

To conclude the work in all its aspects, the behaviour of the similar five-layered waveguides obtained by means of a PE process for all the three different dielectric tensor configurations is determined and compared with Ti process waveguides.

The paper is organized as follows: in Sect. 2 the electromagnetic analysis in a complex formalism for the arbitrary dielectric tensor configuration is summarized. The computer code testing is reported in Sect. 3. The numerical results and the comparison between the Ti:$LiNbO_3$ and H:$LiNbO_3$ waveguides are discussed in Sect. 4.1 and Sect. 4.2, while some possible applications are suggested in Sect. 5

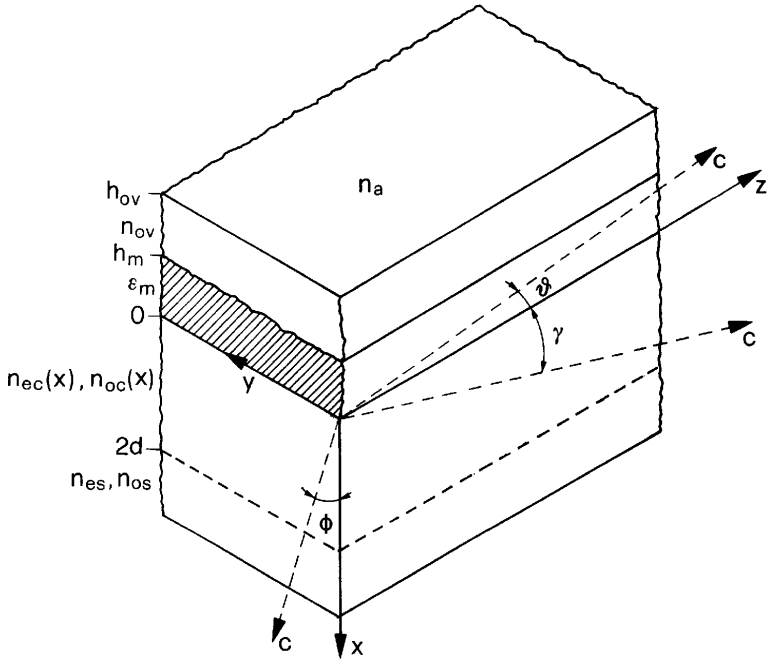

Figure 1. Sketch of the investigated rotated $LiNbO_3$ waveguiding structure.

2. RECALL OF BASIC FORMULATION

The propagation characteristics of guided and leaky modes in anisotropic birefringent waveguides depend on the orientation of the crystal principal axes (a, b, c). The investigated structure, as shown in Fig. 1, is a slab graded-index waveguide with a metal film embedded between the core region and the dielectric overlay.

If the optical c-axis lies in a coordinate plane of the laboratory system, the location of the crystal principal axes can be simply described by means of a suitable unique c-axis angle, defined in the same plane. The polar, the longitudinal and the equatorial configurations are the three interesting cases which occur when the optical c-axis lies in the yz, xy, xz planes, respectively, and θ, ϕ, γ are the corresponding identifying angles (see Fig. 1). Thus, the dielectric tensor component

expressions for the polar (P), longitudinal (L) and equatorial (E) configuration are, respectively:

$$\begin{aligned}
&\varepsilon_{xx} = n_o^2 \\
&\varepsilon_{yy} = n_o^2 \cos^2\theta + n_e^2 \sin^2\theta \\
&\varepsilon_{zz} = n_e^2 \cos^2\theta + n_o^2 \sin^2\theta \\
&\varepsilon_{zy} = \varepsilon_{yz} = (n_e^2 - n_o^2)\sin\theta\cos\theta \\
&\varepsilon_{xy} = \varepsilon_{yx} = \varepsilon_{xz} = \varepsilon_{zx} = 0
\end{aligned} \qquad \text{(P)}$$

$$\begin{aligned}
&\varepsilon_{xx} = n_o^2 \sin^2\phi + n_e^2 \cos^2\phi \\
&\varepsilon_{yy} = n_o^2 \cos^2\phi + n_e^2 \sin^2\phi \\
&\varepsilon_{zz} = n_o^2 \\
&\varepsilon_{xy} = \varepsilon_{yx} = (n_e^2 - n_o^2)\sin\phi\cos\phi \\
&\varepsilon_{xz} = \varepsilon_{zx} = \varepsilon_{zy} = \varepsilon_{yz} = 0
\end{aligned} \qquad \text{(L)}$$

$$\begin{aligned}
&\varepsilon_{xx} = n_o^2 \cos^2\gamma + n_e^2 \sin^2\gamma \\
&\varepsilon_{yy} = n_o^2 \\
&\varepsilon_{zz} = n_e^2 \cos^2\gamma + n_o^2 \sin^2\gamma \\
&\varepsilon_{xz} = \varepsilon_{zx} = (n_e^2 - n_o^2)\sin\gamma\cos\gamma \\
&\varepsilon_{xy} = \varepsilon_{yx} = \varepsilon_{yz} = \varepsilon_{zy} = 0
\end{aligned} \qquad \text{(E)}$$

$\varepsilon_o = n_o^2$ and $\varepsilon_e = n_e^2$ being the ordinary and the extraordinary dielectric permittivity. In the following, the letter "s" or "c" will be added in the subscript in order to indicate substrate or core values, respectively. The plane wave solution of the Maxwell equations, in the hypothesis of the absence of both charge and current sources, gives six equations for the electromagnetic field components. Further statements are the invariance along the y coordinate direction $\partial/\partial y$ and the exponential modal dependence $\exp(-jk_0 nz + j\omega t)$, where $n = n_r + jn_i$ is the complex refractive effective index. In the polar and longitudinal configurations, the first-order differential equation system, which links the electromagnetic field components parallel to the interfaces, leads to hybrid solutions with both ordinary and extraordinary components [4] [10]. In the equatorial dielectric tensor configuration, this system splits into two subsystems, the solutions of which lead to pure TE and TM polarized waves. In particular, the TE modes are the solutions of the well known real Helmholtz wave equation and, for

this reason, will not be a subject of further analysis. Whereas for the TM polarization, the modal solution depends on both the ordinary and extraordinary refractive indices and a detailed investigation becomes necessary.

In the homogeneous and isotropic layers (air, overlay, metal), the differential equation system is analytically solved by assuming an exponential wave behaviour and the field components H_x (proportional to E_y) and H_y in the three media can be easily expressed by means of an overlapping of exponential functions.

When the direction of the x axis is chosen positive, as in Fig. 1, the real part of the air eigenvalue is kept positive so that the field is decreasing away from the core, while the air eigenvalue imaginary part is chosen negative to describe a power flow that is coming into the core or incoming-wave. In the homogeneous substrate, the eigenvalues of the matrix system, for the polar, the longitudinal and equatorial dielectric tensor configuration, are respectively:

$$\lambda_{os} = \pm\sqrt{n^2 - n_{os}^2} \quad \lambda_{es} = \pm\sqrt{\frac{n^2(n_{es}^2\cos^2\theta + n_{os}^2\sin^2\theta)}{n_{os}^2} - n_{es}^2} \qquad \text{(P)}$$

$$\lambda_{os} = \pm\sqrt{n^2 - n_{os}^2} \quad \lambda_{es} = \pm n_{os}\sqrt{\frac{n^2 - n_{es}^2}{n_{es}^2\cos^2\phi + n_{os}^2\sin^2\phi}} \qquad \text{(L)}$$

$$\lambda_s = jn\frac{(n_{es}^2 - n_{os}^2)\sin\gamma\cos\gamma}{n_{os}^2\cos^2\gamma + n_{es}^2\sin^2\gamma} \pm \sqrt{\frac{n^2 - (n_{os}^2\cos^2\gamma + n_{es}^2\sin^2\gamma)}{(n_{os}^2\cos^2\gamma + n_{es}^2\sin^2\gamma)^2}n_{os}^2 n_{es}^2} \qquad \text{(E)}$$

With reference to the polar and the longitudinal configurations, λ_{os} and λ_{es} are the ordinary and extraordinary eigenvalues. If the electromagnetic field profile in the substrate has an exponential dependence $\exp(\lambda x)$, the eigenvalue λ sign is considered negative or positive if the ordinary and extraordinary waves are guided or leaky, respectively. In the case of the equatorial configuration, in the substrate, there is a unique eigenvalue λ_s. The sign choice $\pm$ for the λ_s expression is similar to that made for the two eigenvalues, ordinary and extraordinary, in the cases of polar and longitudinal dielectric tensor configurations [4][10]. In particular, the complex eigenvalue λ_s is chosen by considering that for $n_r^2 > \varepsilon_{xxs}$ the mode is guided: therefore, the only suitable eigenvalue is $\lambda_s \equiv \lambda_s^-$ (i.e. the sign $-$ must be taken in Eq. (E)). In this case, the field decreases along the x direction away

from the core and the power flow is incoming to the core from the substrate (incoming-wave). On the contrary, if $n_r^2 < \varepsilon_{xxs}$ the mode is leaky and the field increases in the substrate away from the core and the opportune eigenvalue is $\lambda_s = \lambda_s^+$. It can be an incoming-wave or an outcoming-wave if the overall imaginary part of the eigenvalue expression is positive or negative, respectiveiy.

In the core diffused region, the system is numerically solved by utilizing Gear's predictor-corrector integration method via the transformation matrix method.

The imaginary part n_i of the refractive effective index n must be chosen as negative in order to assure attenuation along the positive propagation direction z, according to radiation condition, while the real part n_r is chosen as positive by considering only the forward wave.

The boundary conditions for the parallel electromagnetic components at the interfaces $u = -k_0 h_{ov}$, $u = -k_0 h_m$, $u = 0$ and $u = 2k_0 d$ (the latter being the depth for which Ti diffusion or PE exchange effect can be considered exhausted) lead to the eigenvalue equation, the roots of which give the complex propagation constants and are found by using a numerical zoom root-finding algorithm following the tangent plane method optimization strategy.

For guided waves, the total carried power was calculated by integrating the Poynting vector along the transverse coordinate while for leaky waves it is only possible to calculate the power density as a function of depth x from the surface, because the substrate depth must be assumed infinite.

3. COMPUTER CODE VALIDATION THROUGH EXPERIMENTAL INVESTIGATION

The theory, reported in Sect. 2, is applied for implementing a general computer code allowing the investigation of both guided and leaky modes; in particular, it permits the determination of the modal characteristics of all kinds of leaky waves supported by a multilayered anisotropic waveguide, for all the three dielectric tensor configurations. To test the accuracy and the congruency of the computer code, such as the reliability of the obtained results, the calculated effective refractive indices are compared with those obtained via the experimental investigation on two technologically reliable three layered Ti:$LiNbO_3$ waveguides.

The first waveguiding structure under test, WG_1, is a simple Ti:LiNbO$_3$ waveguide, fabricated via the diffusion of 530 Å thick Ti layer at 1000°C in dry atmosphere and for a diffusion time of 10 h on Y-cut substrate. The second tested waveguide, WG_2, is built by diffusing 530 Å thick Ti layer at 1000°C in dry atmosphere into an Y-cut LiNbO$_3$ substrate for a process time of 30 h, then it is annealed at 800°C in wet atmosphere for 1 h.

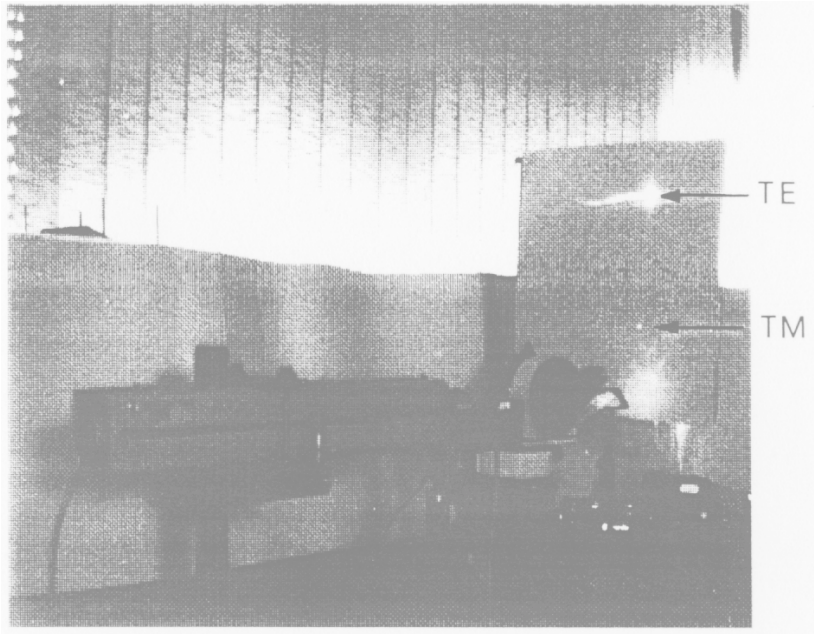

Figure 2. The guided- and leaky-mode measurement set-up.

The dispersion behaviour of the considered waveguides (polar dielectric tensor configuration) was experimentally found by measuring the refractive effective indices for different optical c-axis directions θ. In particular i) guided waves, ii) contra-leaky waves, which leak into the substrate and have an incoming power flow to the core from air, and iii) co-leaky modes, having an incoming power flow to the core from both air and substrate, were excited. The measures were performed by means of a particular set-up, obtained by modifying a classical rutile prism launching configuration, as shown in Fig. 2. More precisely, two digital goniometers, having an angular resolution of 0.001°, were

utilized. The first measures the launching laser angle with respect to the waveguide plane and allows the mode-matching angle evaluation. The second measures the direction of the optical c-axis with respect to the laboratory axes x, y, z, thereby evaluating the azimuth angle θ. The estimated systematic error and the accidental one, made in mode-matching assessment, cause an overall error made in the determination of the refractive effective indices that has a magnitude order of 10^{-3}.

The input laser beam coupling was obtained by using a rutile prism, having ordinary and extraordinary refractive indices $n_{op} = 2.86568$ and $n_{ep} = 2.58385$, respectively, and a base angle equal to $49.45°$. Both the input and the output prisms were assembled on a single support and maintained in line with respect to the laser beam direction. The azimuth angle θ, between the optical c-axis and light propagation direction, was changed by rotating the waveguides with respect to the prisms, as shown in Fig. 3. An example of leaky wave, propagating along the direction $\theta = 75°$ with respect to the optical c-axis, is illustrated in the zoom of Fig. 4. A polarizer lens was located after the laser beam and utilized in order to excite pure TE or TM polarized waves. The alignment of the input prism with the laser beam permits the calculation of the refractive effective indices by substituting, in the Snell law, only the extraordinary refractive index of the rutile prism or the ordinary one. However, the substrate anisotropy of the rotated birefringent waveguide causes the input light change from pure polarized wave to hybrid. The output prism birefringence allows the decoupling of TE and TM components, the light spots of which are projected well separated on the screen, as shown in Fig. 3. In order to obtain the spot of either the single TE or the single TM component, a second polarizer lens was placed after the output prism. Thus, the TE or TM predominant nature of the propagated beam was ascertained by measuring the optical power of both electromagnetic components, by means of a photodetector. The experimental results agree very well with the theory developed in a previous paper [4]. In that work it was theoretically predicted that, for a similar waveguide, the modes keep their polarization, exhibiting predominant TE or TM features in the whole azimuth angle range. Moreover it was asserted that the modes have a stronger hybrid behaviour in the range $10° < \theta < 40°$. The experimental results confirm that the modes having an almost constant shape of the real part of the refractive effective index exhibit a

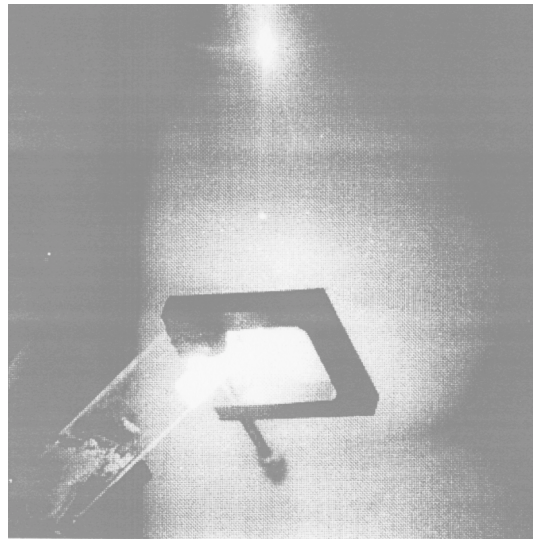

Figure 3. The spots of TE and TM components.

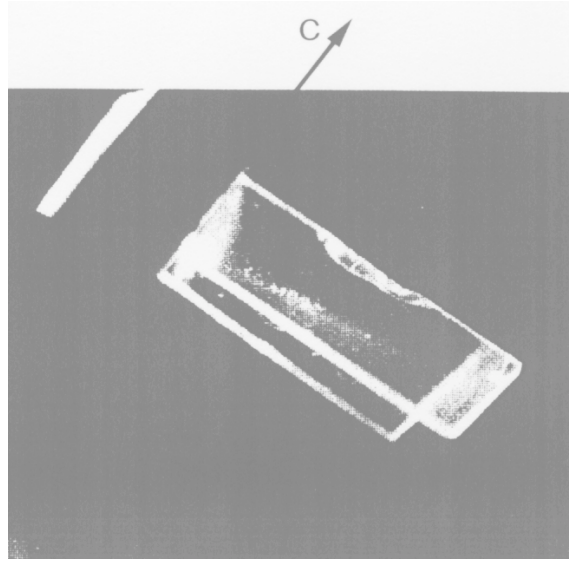

Figure 4. Typical leaky ray propagation. The optical c-axis is parallel to the short side of the sample which lies on a glass holding.

predominant TM nature. On the contrary, the modes characterized by a real part of the refractive effective index that is more strongly varying exhibit a predominant TE nature. For $\theta = 90°$, the modes having the refractive effective index near to n_{os} are pure TM polarized waves, while those having the refractive effective index near to n_{es} are pure TE polarized waves.

The geometrical and physical characteristic parameters of the considered Ti:$LiNbO_3$ waveguiding structures were determined by means of a first computer code procedure, based on the IWKB (Inverse Wentzel-Kramers-Brillouin) method. The computer code input data are the measured waveguide refractive effective indices. The diagnostic was worked out with a laser beam at $\lambda = 0.6328\,\mu$m tilted by $90°$ with respect to the optical c-axis. In fact, the IWKB method can be applied exactly only for $\theta = 0°$ or $\theta = 90°$. In these two cases the TE and TM waves are decoupled. However, the second computer code, based on the theory reported in Sect. 2, allows the dispersion determination, for the azimuth angle θ varying in the whole range from $0°$ to $90°$. The refractive effective indices, calculated by means of the abovementioned theory, are compared with those obtained via the experimental prism-coupling method, for arbitrary c-axis orientations. To confirm that it is possible to diagnose uniaxial waveguides only for $\theta = 90°$, taking into account the c-axis rotation by means of the rotated dielectric tensor configuration formalism, some trials were made. The IWKB method was also approximately applied for the rotated structure and for different optical c-axis orientations. In these cases new substrate extraordinary refractive index values were considered to take into account the rotation of the dielectric constant tensor. The substrate extraordinary indices were obtained considering the substrate eigenvalue expression.

For both tested waveguides, the Ti:$LiNbO_3$ core in-depth semigaussian refractive index profile can be described by means of the same expression $n_{e,o}(x) = n_{es,os} + \Delta n \exp[-(x/d_{eo})^2]$, where $n_{es} = 2.202$ and $n_{os} = 2.286$ are the extraordinary and ordinary refractive indices, respectively.

The IWKB characterization, developed for $\theta = 90°$, leads to the calculation, for the first tested waveguide WG_1, of the Ti-diffusion extraordinary and ordinary depths $d_e = 3.94\,\mu$m and $d_o = 5.24\,\mu$m and of the extraordinary and ordinary refractive index changes at the sur-

face $\Delta n_e = 0.019$ and $\Delta n_o = 0.010$. These parameters are employed as input data in the computer code which analyzes the anisotropic waveguide having an arbitrary optical c-axis direction.

Fig. 5 shows the variation of the real part n_r of the refractive effective index versus the azimuth angle θ. The full curves refer to the simulation results and the circles indicate the experimental values. The label "G" indicates the guided modes while the leaky modes are labelled with the symbol "L". Three of the experimentally identified guided waves exhibit a transition angle from guided to leaky modes $\theta = 3° \div 15°$. For this optical c-axis orientation, the refractive effective indices of guided modes become smaller than the substrate ordinary refractive index $n_{os} = 2.286$ which is represented with the broken curve $C_{os}(\theta)$. The leaky mode dispersion behaviour is similar to that previously calculated for a five layered structure having the same anisotropic substrate [4].

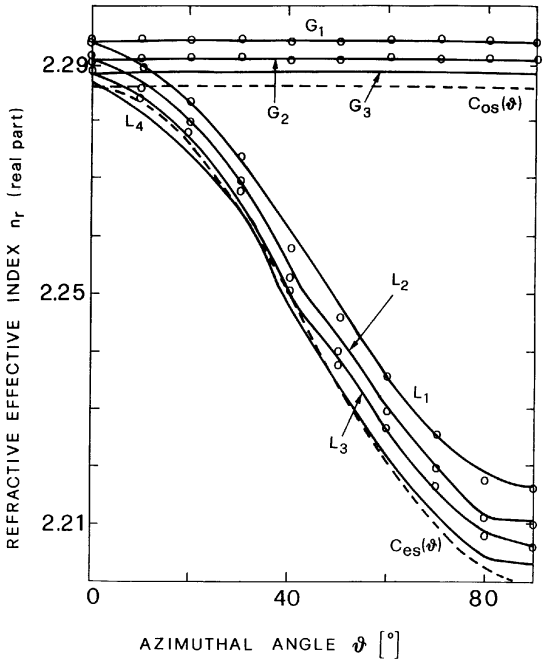

Figure 5. Variation of the real part n_r of the refractive index versus the azimuth angle θ, for the WG_1 waveguide. The circles indicate experimental data.

The mapping of the wavefunction profile of electromagnetic field components H_x and H_y, calculated by means of our computer code, confirms the illustrated dispersion curves. As an example, Fig. 6 shows the in-depth distribution of the H_x (broken curve) and H_y (full curve) components of the electromagnetic field for $\theta = 30°$, of (a) the leaky mode L_1 having the real part of the simulated refractive effective indices $n_r = 2.27368$; (b) the leaky mode L_2 having $n_r = 2.26984$, (c) the leaky mode L_3 having $n_r = 2.26684$. The number of zeroes of the wavefunction profile H_x and H_y along the x coordinate, increases with the modal order for both guided and leaky modes. The simulated H_x electromagnetic field component is much greater than the H_y. This predominant TE nature is experimentally confirmed. The L_1 leaky mode H_x profile exhibits one principal peak and four secondary ones due to the leakage phenomenon, while the L_2 and L_3 modes have two and three H_x principal peaks respectively, the number of secondary peaks becoming two and one. For the H_y component, the leakage phenomenon is more evident, the wavefunction profile oscillates and slightly increases when x increases, the number of peaks is nine for L_1, ten for both L_2, L_3.

Other complex solutions of Maxwell's equations, having a leaky dispersion behaviour like that of the guided G_3 mode or that of the leaky L_4 mode, were found via the computer code simulation. These other leaky modes have a smaller real part of the refractive effective indices and their curves are not illustrated in Fig. 5. The modes whose dispersion curve is like that of G_3 have a predominant TM (ordinary) nature. The real part of their refractive effective indices is smaller than the $C_{os}(\theta)$ broken curve so they have an almost completely leaky nature. On the contrary the modes having a dispersion curve like that of L_4 mode have a predominant TE (extraordinary) nature. The real part of their refractive effective index is smaller than the $C_{es}(\theta) = n_{os}n_{es}/\sqrt{\varepsilon_{zzs}(\theta)}$, that is the other broken curve depicted in Fig. 5, below which the extraordinary electromagnetic field component also assumes a leaky behaviour into the substrate. Therefore these modes have a completely leaky nature, having both the ordinary and extraordinary electromagnetic components that leak. Moreover, these modes have a greater modal order, so they exhibit a small power flow along the z propagation direction. The wavefunction profile of the electromagnetic components H_x and H_y along the x coordinate of the leaky L_4 mode, having $n_r = 2.264800$ for $\theta = 30°$, is shown

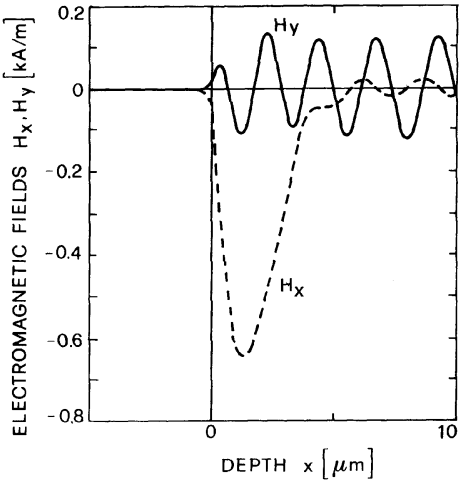

(a)

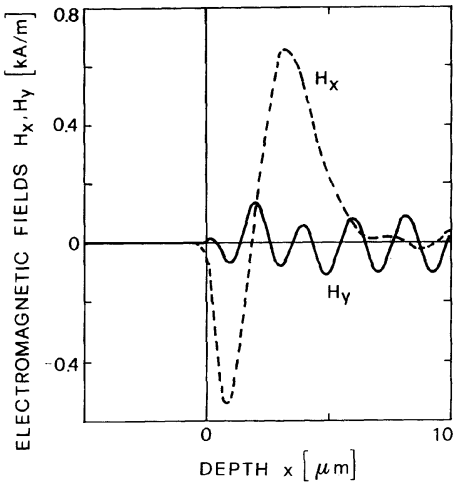

(b)

Figure 6. Mappings of the field components H_x and H_y, for $\theta = 30°$, of (a) the leaky mode L_1, (b) the leaky mode L_2.

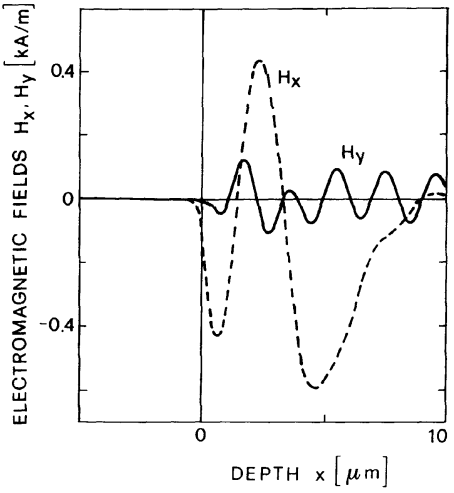

(c)

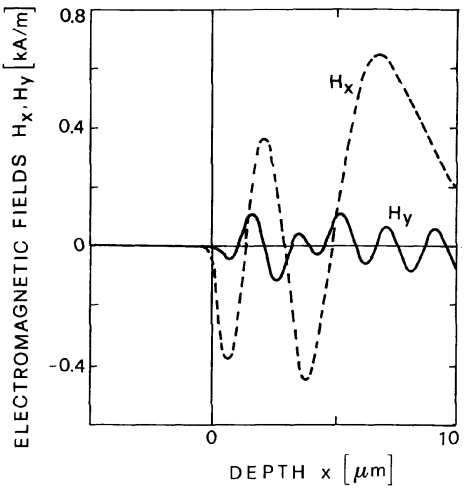

(d)

Figure 6. Mappings of the field components H_x and H_y, for $\theta = 30°$, of (c) the leaky mode L_3, and (d) the leaky mode L_4.

in Fig. 6d. The predominant component H_x exhibits a stronger leaky behaviour. Finally, the leaky modes which are not reported in Fig. 5 have the real parts of the refractive effective indices close to each other. In fact, in our experiment, a corresponding very weak, almost continuous, light spot was observed and it was impossible to separate with any high degree of accuracy the mode matching angle of these modes. The goal of our investigation is reached because the computer code procedure results agree very well with the experimental ones, being practically indistinguishable. As an example, the real parts of the simulated refractive effective indices, for $\theta = 0^\circ$, are: 2.29395, 2.29382, 2.29093, 2.29070, 2.28847, for L_1, G_1, L_2, G_2, L_3, while the corresponding measured values are: 2.294, 2.293, 2.291, 2.290, 2.289. The differences are in the limits of the measurement error.

For the second waveguide WG_2, the calculated values using the IWKB method, for $\theta = 90^\circ$, are: Ti-diffusion characteristic extraordinary $d_e = 6\,\mu$m and ordinary $d_o = 9.9\,\mu$m depths, the extraordinary and ordinary refractive index changes at the surface $\Delta n_e = 0.011$ and $\Delta n_o = 0.008$. The variation of the real part n_r of the refractive effective index by increasing the azimuth angle θ is similar to that shown for the previous waveguide and is shown in Fig. 7.

Also in this case the differences between simulated and measured refractive effective indices are in the limits of the measurement error. As an example, the real parts of the simulated refractive effective indices, for $\theta = 90^\circ$, are: 2.29303, 2.29148, 2.29007, 2.21075, 2.20790, 2.20548, for G_1, G_2, G_3, L_1, L_2, L_3, while the corresponding measured values are: 2.293, 2.291, 2.290, 2.210, 2.207, 2.205. The guided G_4, and L_4 modes were found via computer code simulation, while the similar others, having smaller refractive effective indices, are not reported. In conclusion, the code results can be utilized in order to develop accurate theoretic investigations of other waveguides.

4. NUMERICAL RESULTS

4.1 Ti:LiNbO$_3$ Waveguide in the Equatorial Dielectric Tensor Configuration: Numerical Simulation

The performance of typical Ti:LiNbO$_3$ waveguiding structures is simulated via our computer code. The waveguide parameters chosen in this and following simulations are: $d_e = d_o = d = 1\,\mu$m,

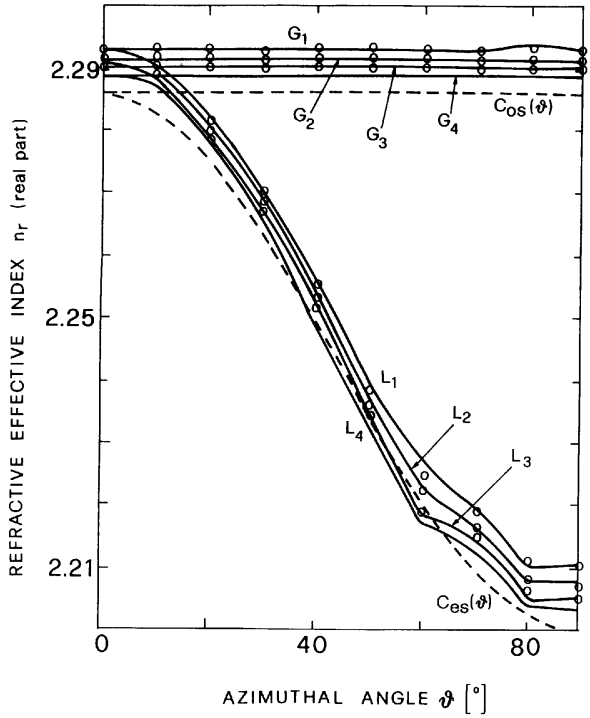

Figure 7. Variation of the real part n_r of the refractive effective index versus the azimuth angle θ, for the WG_2 waveguide. The circles indicate experimental data.

$\Delta n_e = \Delta n_o = \Delta n = 0.04$. The overlay constituted of a SiO_2-Ta_2O_5 layer has a thickness equal to $h_{ov} - h_m = 0.38\,\mu$m, and a variable refractive index depending on the composition ratio. The metal layer, $h_m = 0.02\,\mu$m thick, is commonly made of gold, silver, aluminium or nickel which exhibit complex permittivity at $\lambda = 0.6328\,\mu$m equal to $\varepsilon_{Au} = -10.22 - j0.96$, $\varepsilon_{Ag} = -16.3 - j0.52$, $\varepsilon_{Al} = -47.56 - j16.8$, $\varepsilon_{Ni} = -10.44 - j15.2$, respectively.

Fig. 8 (a) depicts the variation of the real part n_r of the refractive effective index versus the equatorial angle γ, while Fig. 8 (b) illustrates the attenuation constant $\alpha\,(\mathrm{dB/cm})$, for a waveguide with a silver layer and an overlay having refractive index $n_{ov} = 2.1$. The subscript indicates the number of zeroes of the wavefunction profile H_y along

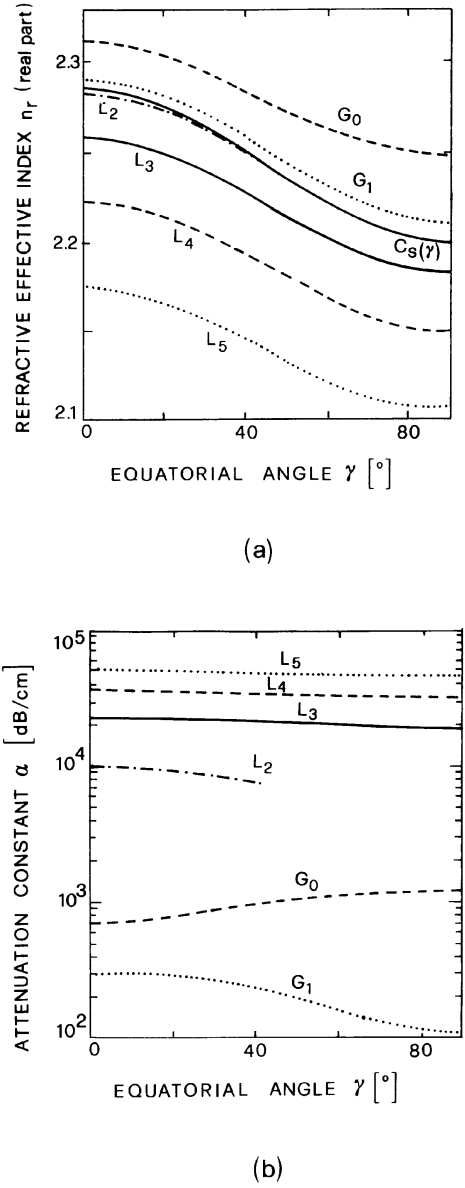

Figure 8. (a) Dispersion curves and (b) attenuation constant α versus the equatorial angle γ for the Ti:LiNbO$_3$ waveguide having Ag layer.

the x coordinate. The curve $C_s(\gamma) = \sqrt{\varepsilon_{xxs}(\gamma)}$ is also reported. It defines the transition region from guided to leaky propagation. For both calculated leaky and guided modes, the real part of the refractive effective index decreases by increasing γ, and it has almost the same behaviour. In the whole γ range,the G_0 and G_1 modes, having respectively $n_r = 2.31198$ and $n_r = 2.29027$ for $\gamma = 0°$, remain guided. Only a section of the curve which pertains to the first leaky mode L_2, having $n_r = 2.28252$ for $\gamma = 0°$, is drawn because for $\gamma > 40°$ it overlaps the curve $C_s(\gamma)$. The $C_s(\gamma)$ region is critical for the numerical convergence of the method and this occurrence can be explained by considering the eigenvalue expression. In Fig. 8 (b) the losses of guided modes show various behaviours: the G_0 mode attenuation constant increases from about 7.2×10^2 dB/cm for $\gamma = 0°$ to 1.2×10^3 dB/cm for $\gamma = 90°$. On the contrary, the G_1 mode attenuation constant is lower than that of the G_0 mode, in fact it decreases from 3.0×10^2 dB/cm at $\gamma = 0°$ to only 1.1×10^2 dB/cm at $\gamma = 90°$. The leaky modes, in the equatorial dielectric tensor configuration, are described by means of a unique eigenvalue. They have no bounded electromagnetic field component; therefore, the leaky modes exhibit losses of about two orders of magnitude greater than those of the guided modes, slightly decreasing as γ increases. As an example the L_5 mode, having $n_r = 2.17460$ for $\gamma = 0°$ and $n_r = 2.10586$ for $\gamma = 90°$, suffers an attenuation of 5.2×10^4 dB/cm for $\gamma = 0°$ and of 4.5×10^4 dB/cm for $\gamma = 90°$.

The dispersion curves and the leaky or guided nature of the various modes are confirmed by the electromagnetic field pattern along the transverse coordinate x. As an example, Fig. 9 illustrates the mappings of the electromagnetic field component H_y pertaining to the six modes which propagate in the Ti:$LiNbO_3$ waveguide with Ag layer, for the orientation of the crystal optical axis $\gamma = 10°$. The number of zeroes along the x coordinate increases as the modal order increases.

The dispersion curves and the loss shapes for the waveguides having a gold, aluminium and nickel layer, are depicted in Figs. 10–12, respectively. In particular, the waveguide with Au film (Fig. 10), has a modal behaviour like that shown in Fig. 8. In fact it supports two guided modes and four leaky modes and its dispersion curves show a decreasing shape. The G_0 mode has, for small angle values, a surface plasma mode nature; in fact the real part of its refractive effective index is $n_r = 2.33118$ for $\gamma = 0°$, then, for $\gamma > 10°$ it becomes

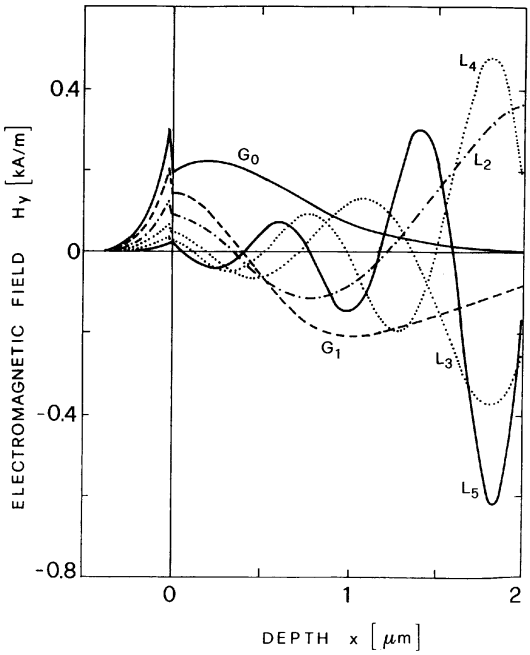

Figure 9. In depth distribution of the H_y electromagnetic field component of the six modes which propagate in the Ti:LiNbO$_3$ waveguide with Ag layer, for $\gamma = 10°$.

guided. As an example, for $\gamma = 30°$ the real part of the effective refractive index is $n_r = 2.31678$. The n_r variation range is kept over the value 2.1 which is the refractive index of the overlay, therefore the curve of the leaky L_5 mode is limited to the range $0° < \gamma < 20°$, the refractive effective index of this mode being $n_r = 2.107694$ for $\gamma = 20°$. The guided G_0 mode has an attenuation constant α which slowly increases, changing from 5.1×10^3 dB/cm to 6.1×10^3 dB/cm when γ varies from $0°$ to $90°$. On the contrary, the G_1 mode attenuation constant is decreasing, as occurs for all other modes, changing from 6.2×10^2 dB/cm for $\gamma = 0°$ to 2.4×10^2 dB/cm for $\gamma = 90°$. The waveguides having the Al (Fig. 11) and Ni (Fig. 12) film exhibit other likenesses. They support only one guided mode and four leaky modes. For both these metal films, the dispersion behaviour is quite similar to that of the previous cases (Ag and Au), however there are

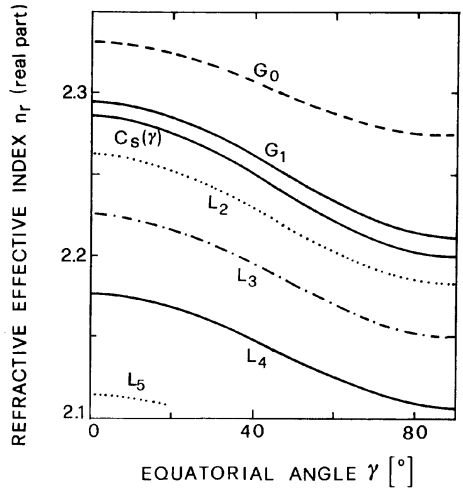

(a)

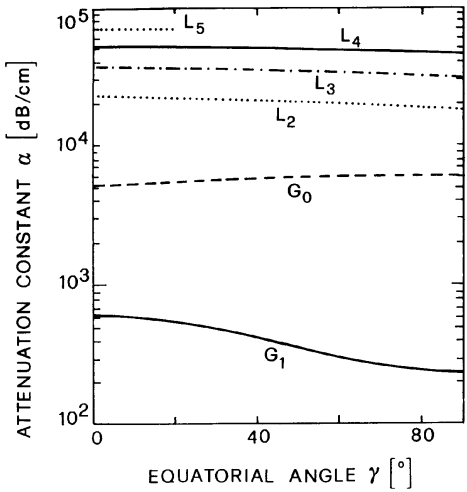

(b)

Figure 10. (a) Dispersion curves and (b) attenuation constant α versus the equatorial angle γ for the Ti:$LiNbO_3$ waveguide having Au metal layer.

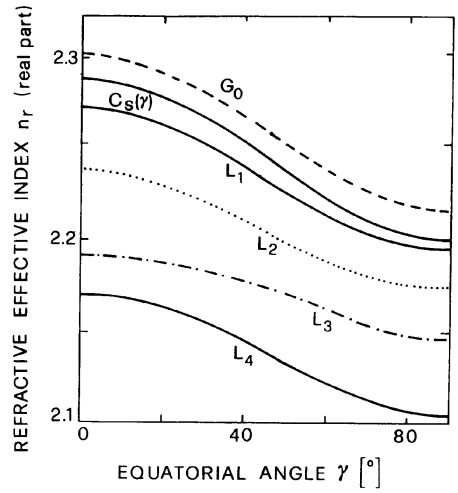

Figure 11. (a) Dispersion curves and (b) attenuation constant α versus the equatorial angle γ for the Ti:LiNbO$_3$ waveguide having Al metal layer.

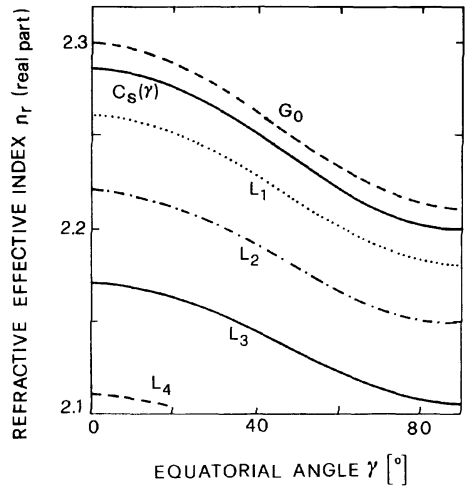

Figure 12. (a) Dispersion curves and (b) attenuation constant α versus the equatorial angle γ for the Ti:$LiNbO_3$ waveguide having Ni metal layer.

a few differences. The attenuation constant of the fundamental G_0 mode, for the Al film, is always growing as γ increases: in fact, its value is $\alpha = 1.3 \times 10^3\,\mathrm{dB/cm}$ and $\alpha = 3 \times 10^3\,\mathrm{dB/cm}$ for $\gamma = 0°$ and $\gamma = 90°$, respectively. On the contrary, for the waveguide with Ni film, the G_0 attenuation constant is almost constant and equal to $\alpha \cong 6.6 \times 10^3\,\mathrm{dB/cm}$ until $\gamma = 30°$ and, then, it decreases assuming the value $\alpha = 2.8 \times 10^3\,\mathrm{dB/cm}$ for $\gamma = 90°$.

The effects of the overlay refractive index variation on waveguide modal behaviour can be very heavy. Fig. 13 shows the curves of: (a) the real part of the complex refractive effective index and (b) the attenuation constant α as a function of the overlay refractive index n_{ov}, for the crystal optical c-axis orientation $\gamma = 10°$, and an Ag metal layer. The real part of the refractive effective index of the fundamental mode G_0 assumes a constant trend until $n_{ov} = 2.1$, then the shape is significantly modified by the presence of a dielectric layer having a higher index value. It strongly increases until the mode transforms into a surface plasma wave. In fact, the real part of the refractive effective index varies from $n_r = 2.3098$ for $n_{ov} = 2.1$ to $n_r = 2.5153$ for $n_{ov} = 2.5$. On the contrary, the other modes, in the considered n_{ov} range, show slighter behaviour. The curve which refers to the mode G_1, for n_{ov} values less than 2.1, has not been drawn because it is practically coincident with the value of the curve $C_s(\gamma)$ for $\gamma = 10°$.

The attenuation constant curves are practically insensitive to the overlay refractive index change from $n_{ov} = 1$ until $n_{ov} \cong 2$. In this range the attenuation constants of the guided modes are almost three orders of magnitude less than that of the leaky modes. By increasing the overlay refractive index n_{ov}, for values greater than 2.1, the G_0 mode attenuation constant rapidly increases, changing from $7.4 \times 10^2\,\mathrm{dB/cm}$ to $2.2 \times 10^3\,\mathrm{dB/cm}$ when the overlay refractive index changes from 2.1 to 2.5. The G_1 loss curve oscillates when n_{ov} increases, it exhibits an attenuation peak of $2.4 \times 10^2\,\mathrm{dB/cm}$ for $n_{ov} = 2.1$ then it decreases until a minimum of $27\,\mathrm{dB/cm}$ for $n_{ov} = 2.35$ and for greater n_{ov} values it increases again. The attenuation curve of the leaky L_2 mode significantly decreases: the attenuation constant changes from $1.0 \times 10^4\,\mathrm{dB/cm}$ to $1.8 \times 10^2\,\mathrm{dB/cm}$ when the overlay refractive index varies from 2.1 to 2.5. The L_5 mode exhibits a different behaviour, while the L_3 and L_4 modes have a smoother variation for $n_{ov} > 2.1$.

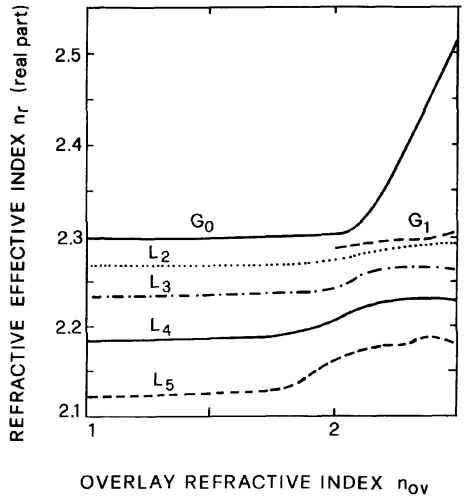

Figure 13. (a) Real part of the refractive effective index and (b) attenuation constant α as a function of the overlay refractive index n_{ov}, for $\gamma = 10°$, Ag metal layer.

These numerical results and those obtained for the same structure having polar and longitudinal dielectric tensor configurations [4,10] lead to the conclusion that new transition angles from guided-to-leaky modes exist. In fact, the migration leaky-to-guided mode can occur also when the optical c-axis is oriented near the x axis. If the Ti waveguide having an Ag metal layer, suffers a rotation of the optical c-axis from the xz plane to the xy one, the modes G_0 and G_1, which are guided for $\gamma \cong 90°$ in the equatorial dielectric tensor configuration, suddenly become leaky L_1^1 and L_2^1 for $\phi \cong 0$ in the longitudinal one [10]. This phenomenon can be explained by considering that these modes change their nature from pure TM guided modes to hybrid ones with the ordinary component that leaks into the substrate. On the contrary the L_4 mode keeps its full leaky behaviour because it transforms from a pure TM leaky mode having no bounded component into the L_4^2 mode having both ordinary and extraordinary components that leak into the substrate, when the orientation of the optical c-axis changes from the equatorial to the longitudinal dielectric tensor configuration. However, the attenuation constant does not exhibit any peak in the transitions.

4.2 Performance of PE Waveguide Having Arbitrary Dielectric Tensor Configuration

To conclude our investigation, here we report the characteristics of c-rotated waveguides made by proton exchanged technology H:LiNbO$_3$. According to the literature data [11], the typical PE technology parameters assumed in the following analysis are: the positive high extraordinary index change at the surface $\Delta n_e = 0.12$, the negative ordinary index change at the surface $\Delta n_0 = -0.03$ and the extraordinary and ordinary exchange depth $d = d_e = d_o = 3\,\mu$m. The calculated dispersion behaviour is quite different with respect to that of the Ti:LiNbO$_3$ waveguides.

Fig. 14 (a) depicts the variation of the real part of the refractive effective indices and (b) the attenuation constant α curves of the modes supported by a H:LiNbO$_3$ waveguide having a silver layer and $n_{ov} = 2.1$ versus the equatorial angle γ. This figure reports the substrate transition curve $C_s(\gamma) = \sqrt{\varepsilon_{xxs}(\gamma)}$. Differently from that which occurs for Ti:LiNbO$_3$ waveguides all the modes have leaky characteristics for $\gamma = 0°$. In fact the real part of their refractive effective indices is smaller than the $C_s(\gamma)$. Fig. 14 reports also the

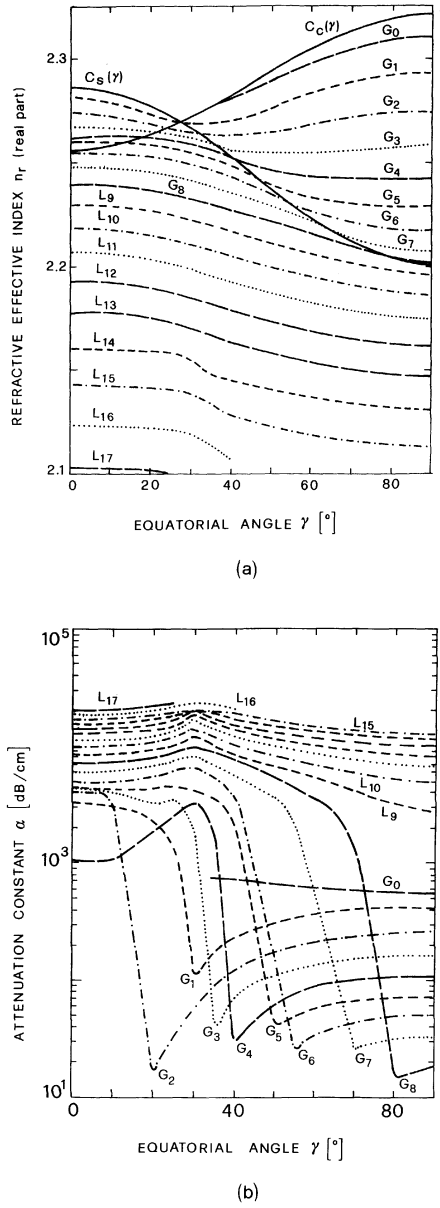

Figure 14. (a) Real part n_r of the refractive index and (b) attenuation constant α versus the equatorial angle γ for the H:$LiNbO_3$ waveguide having a silver layer and $n_{ov} = 2.1$.

core transition curve $C_c(\gamma) = \sqrt{\varepsilon_{xxc}(\gamma)}$. For a step-index and lossless waveguide, by considering a refractive effective index having a real value, the $C_s(\gamma)$ and $C_c(\gamma)$ curves define four regions in which the eigenvalues, calculated in the substrate and the core, can have pure imaginary value or can have a non zero real part. Only in the region a) defined by $C_s(\gamma) < n_{ef} < C_c(\gamma)$ do the eigenvalues describe guided modes, having pure imaginary values in the core and a negative real part in the substrate. For the whole $n_{ef} < C_s(\gamma)$ range, the chosen substrate eigenvalue describes a leaky field behaviour along the x coordinate. But, while for the region b) $C_c(\gamma) < n_{ef} < C_s(\gamma)$ the core eigenvalue has a real part, in the third region c) $n_{ef} < C_c(\gamma)$ and $n_{ef} < C_s(\gamma)$, the core eigenvalue has a pure imaginary value. The first nine leaky modes transform into guided modes when they reach the $C_s(\gamma)$ curve. Finally, in the fourth region d) $n_{ef} > C_c(\gamma)$ and $n_{ef} > C_s(\gamma)$ no solution was found. The angle value, for which the transition occurs, increases as the modal order increases. The modes labelled with the symbol "G_i" are those which change their nature from leaky to guided, on the contrary the modes which maintain their leaky nature in the whole γ range are indicated with the letter "L". As an example, the first leaky mode transforms into the fundamental G_0 mode near $\gamma = 35°$, where the real part of its refractive effective index is $n_r = 2.27722$. For the ninth leaky mode G_8, the transition angle is $\gamma \cong 75°$. For $0 < \gamma < 35°$, the leaky mode which transforms into the fundamental guided G_0 mode is not drawn: in this range, no solution is found via the computer code simulation because the searched dispersion curve practically overlaps the curve $C_s(\gamma)$. All the modes from L_9 until L_{17} show a slight variation of the real part of the refractive effective index with respect to γ. For these modes the attenuation constants increase as the modal order increases in the whole γ range. As an example, for $\gamma = 0°$, the attenuation constant of the L_9 leaky mode having the real part of the refractive effective index $n_r = 2.22954$ mode is $\alpha = 8.4 \times 10^3$ dB/cm while for the L_{17} leaky mode having $n_r = 2.10268$ is $\alpha = 2.0 \times 10^4$ dB/cm. The losses of the leaky modes which transform into guided modes strongly decrease, reaching a minimum near the transition angles. The wave G_1 for $\gamma = 25°$ is leaky; it has the real part of the refractive effective index $n_r = 2.26675$ and the attenuation constant $\alpha = 2.3 \times 10^3$ dB/cm. Then, for $\gamma = 30°$ it becomes a guided mode having $n_r = 2.26734$ and its attenuation constant drastically decreases to $\alpha = 1.1 \times 10^2$ dB/cm.

The transition from leaky to guided modes when the refractive effective indices reach the $C_s(\gamma)$ curve values is confirmed by the evolution of the in-depth profile of the electromagnetic field versus the equatorial angle. Fig. 15 (a) maps the field component H_y of the fundamental G_0 mode which propagates in the H:$LiNbO_3$ waveguide for the orientation of the crystal optical axis $\gamma = 30°$ (broken curve) and $\gamma = 50°$ (full curve). For $\gamma = 50°$ the field shows the typical shape of the guided mode while for $\gamma = 30°$ the formation of a secondary negative peak is already evident due to the nearness of the mode to the transition region $C_s(\gamma)$. In Fig. 15 (b) the H_y electromagnetic field mappings of the G_2 mode (broken curve) having for $\gamma = 20°$, $n_r = 2.26735$ and of the G_5 mode (full curve) having for $\gamma = 30°$, $n_r = 2.254362$, are shown. They belong to the two different regions b) and c); however, both the mappings show a typical leaky nature.

This section is closed by illustrating the characteristics of H:$LiNbO_3$ waveguides in the other two c-axis configurations, the longitudinal and the polar ones, in which the modes are hybrid. The modal behaviour of the PE waveguide having a longitudinal dielectric tensor configuration is shown in Fig. 16. There, (a) the dispersion curves and (b) the attenuation constant α curves of the H:$LiNbO_3$ waveguide having a silver layer and $n_{ov} = 2.1$ versus the longitudinal angle ϕ are illustrated. For the longitudinal and the polar configuration, the hybrid electromagnetic field expression is the sum of both the ordinary and extraordinary components. Therefore, for a step refractive index profile and lossless waveguide having a longitudinal dielectric tensor configuration, by assuming the refractive effective index having a real value, there are four curves defining the regions in which the eigenvalues, calculated in the substrate and in the core, can have pure imaginary or real values. These curves have constant values in the whole ϕ range, being: $C_{ec}(\phi) = n_{es} + \Delta n_e$, $C_{os}(\phi) = n_{os}$, $C_{oc}(\phi) = n_{os} + \Delta n_o$, $C_{es}(\phi) = n_{es}$. Of course, also in this case, in each region the modes can have the extraordinary and ordinary components with different behaviour and very different amplitude. As an example, in the range $C_{ec}(\phi) < n_{ef} < C_{os}(\phi)$ the modes can be considered guided although only the extraordinary component is guided (the ordinary component is evanescent in the core). For $C_{os}(\phi) < n_{ef} < C_{oc}(\phi)$ the extraordinary component is guided while ordinary component is evanescent in the core and leaky into the substrate. For

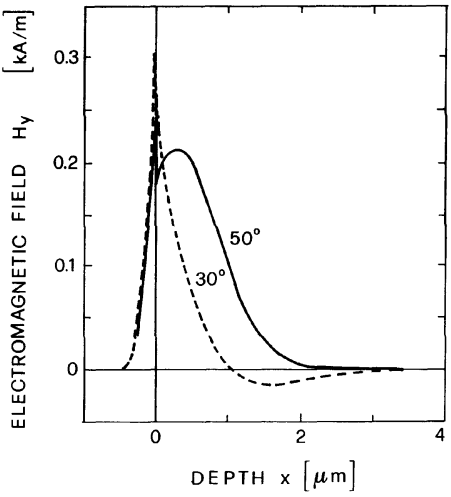

(a)

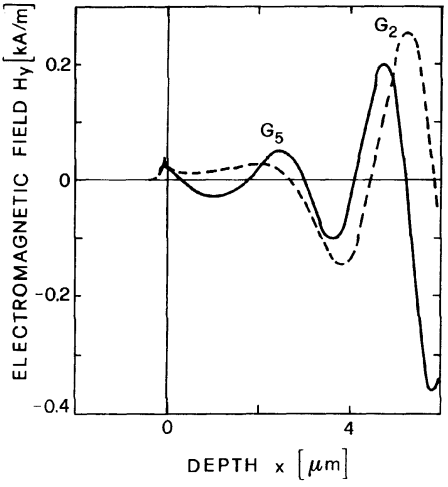

(b)

Figure 15. Mapping of the field component H_y for: (a) the fundamental G_0 guided mode of the H:LiNbO$_3$ waveguide for $\gamma = 30°$ and $\gamma = 50°$; (b) the G_2 leaky mode of the H:LiNbO$_3$ waveguide for $\gamma = 20°$ and the G_5 leaky mode for $\gamma = 30°$.

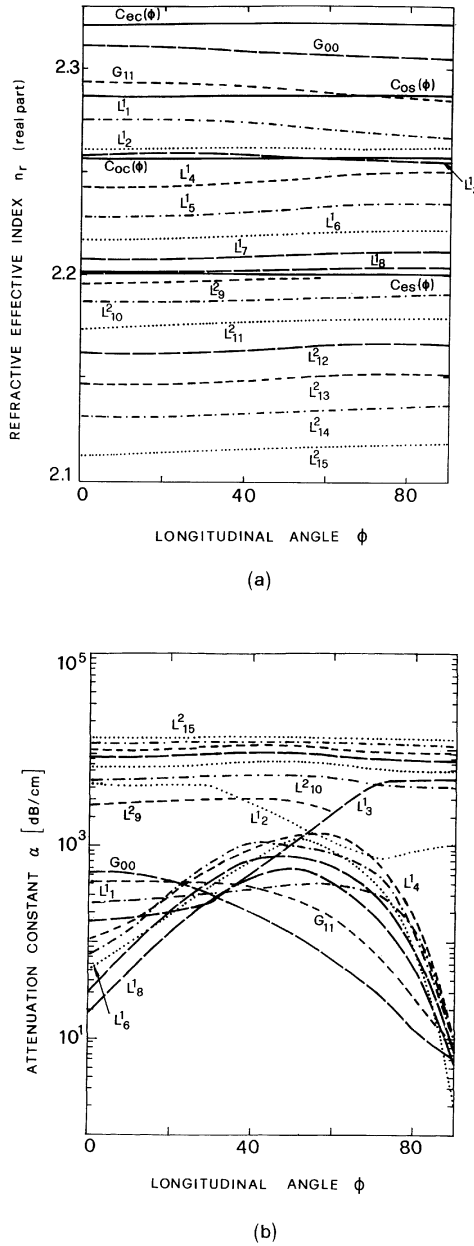

Figure 16. (a) Real part n_r of the effective refractive index and (b) attenuation constant α versus the longitudinal angle ϕ for the H:$LiNbO_3$ waveguide having a silver layer and $n_{ov} = 2.1$.

$C_{oc}(\phi) < n_{ef} < C_{es}(\phi)$ both the core eigenvalues have pure imaginary values; the extraordinary component is guided while the ordinary component leaks into the substrate. For $n_{ef} < C_{es}(\phi)$ both extraordinary and ordinary components leak into the substrate. As was found in the case of the equatorial dielectric tensor configuration, the most important curves are those which refer to the substrate eigenvalue transition $C_{os}(\phi) = n_{os}$ and $C_{es}(\phi) = n_{es}$. The double subscript attached to the label "G", which refers to hybrid, guided (or almost guided) modes, indicates the number of zeroes of the wavefunction profiles H_x and H_y along the x-coordinate, in the core region. The label "L^1" indicates a leaky mode having only the ordinary component that leaks into the substrate, while the symbol "L^2" refers to leaky modes with both the ordinary and extraordinary components leaking into the substrate. The subscript of the leaky modes characterizes only the leaky mode order. However, as for the equatorial configuration, the number of zeroes of the leaky modes increases by decreasing the value of the real part of the refractive effective index. For $\phi > 60°$ the refractive effective index curve of the leaky L_9^2 mode is not reported. In fact, the region near the extraordinary refractive index of the substrate $C_{es} = 2.202$, as that near the ordinary refractive index $C_{os} = 2.286$, is critical for the convergence of numerical method. The real part n_r of the refractive effective index of all the modes varies slowly as for the Ti:LiNbO$_3$ waveguide in the same configuration [10]. But, while for the Ti:LiNbO$_3$ waveguide [10] the real part of the refractive effective index of all the modes increases by increasing the longitudinal angle ϕ, for the H:LiNbO$_3$ waveguide the refractive effective index of the G_{00}, G_{11}, L_1^1, L_3^1 modes decreases by increasing the longitudinal angle ϕ. For the other modes, the real part of the effective refractive index increases or exhibits an intermediate behaviour. As an example, the real part of the refractive effective index of the fundamental mode G_{00} is $n_r = 2.31074$ for $\phi = 0°$, while it becomes $n_r = 2.30470$ for $\phi = 90°$. On the contrary, the real part of the refractive effective index of the leaky L_{15}^2 mode is $n_r = 2.11336$ for $\phi = 0°$, while it becomes $n_r = 2.11846$, for $\phi = 90°$. However the differences of modal dispersion between the H:LiNbO$_3$ and Ti:LiNbO$_3$ waveguides are more evident for the equatorial configuration and, as will be shown, for the polar one. In fact, for these configurations, the different value of the extraordinary and ordinary surface index change more strongly influences the behaviour of the transition curves C_{oc}, C_{ec}, C_{os}, C_{es}, and of

the corresponding regions.

The guided G_{00} and G_{11} modes have losses which decrease as the longitudinal angle ϕ increases. More precisely the G_{00} mode attenuation constant α is equal to 5.5×10^2 dB/cm for $\phi = 0°$ and decreases to $\alpha = 6.3$ dB/cm for $\phi = 90°$. The attenuation constant curve of the leaky "L^1" modes exhibit an attenuation peak in the range $\phi = 50° \div 70°$, while the losses of the leaky "L^2" modes assume an almost constant value by increasing the longitudinal angle ϕ. The mode L_6^1 having for $\phi = 0°$ the refractive effective index $n_r = 2.21719$ and the attenuation constant $\alpha = 49$ dB/cm, for $\phi = 50°$ has $n_r = 2.21981$ and exhibits an attenuation constant peak $\alpha = 1.3 \times 10^3$ dB/cm, then for $\phi = 90°$ the refractive effective index is $n_r = 2.22339$ and the attenuation constant is $\alpha = 2.0$ dB/cm. In the case of Ti-diffused waveguide [10], the attenuation constants of guided modes increase by increasing the longitudinal angle ϕ. The attenuation constant curve of L_1^1 mode monotonically increases, those of L_0^1, L_3^2 and L_4^2 waves slowly decrease and that of L_2^1 mode exhibits an attenuation peak at $\phi \cong 40°$.

For the PE waveguide having a longitudinal dielectric tensor configuration, the mappings of the H_x and H_y field components have the typical profiles of the guided or leaky modes like those previously shown in Fig. 9.

The dispersion curves of the H:$LiNbO_3$ waveguide having a silver layer and $n_{ov} = 2.1$ versus the azimuth angle θ, when the dielectric tensor exhibits a polar configuration, are shown in Fig. 17 (a). The transition curves are $C_{ec}(\theta) = n_{oc}n_{ec}/\sqrt{\varepsilon_{zzc}(\theta)}, C_{os}(\theta) = n_{os}, C_{oc}(\theta) = n_{os}+\Delta n_o, C_{es}(\theta) = n_{os}n_{es}/\sqrt{\varepsilon_{zzs}(\theta)}$. Consideration about the bounded or leaky nature of the ordinary and extraordinary components can be made as in the previous cases. All the modes have leaky characteristics for $\theta = 0°$. The real part of the refractive effective index of the first mode G_{00}, for $\theta = 0°$ is $n_r = 2.28072$ and it is leaky L^2 type, with both the components, ordinary and extraordinary, which leak into the substrate. Then, for $\theta \cong 22°$, the G_{00} mode refractive effective index reaches the migration curves $C_{es}(\theta)$ and there it transforms into a leaky mode with only the ordinary component that leaks. Finally, for $\theta = 55°$, when the real part of the refractive effective index reaches $C_{os}(\theta) = n_{os} = 2.286$, it becomes an almost guided mode having the guided extraordinary component and the evanescent ordinary component in the core. From the second order mode until the

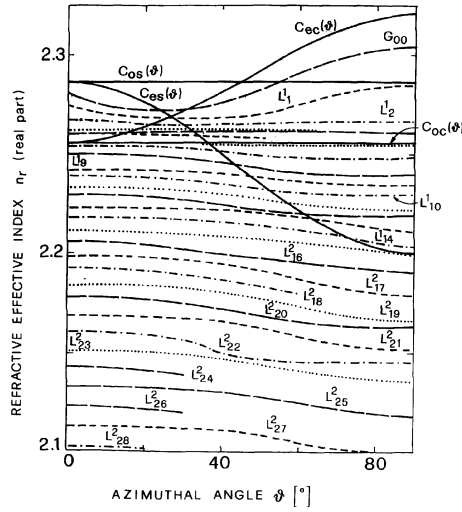

(a)

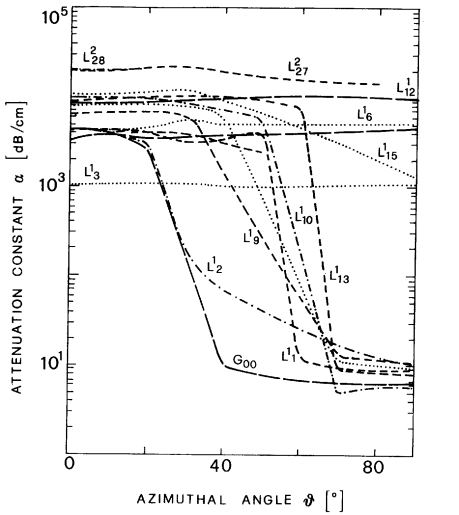

(b)

Figure 17. (a) Real part n_r of the effective refractive index and (b) attenuation constant α versus the azimuthal angle θ for the H:LiNbO$_3$ waveguide having a silver layer and $n_{ov} = 2.1$.

mode L_{14}^1 a transition from leaky L^2 type to L^1 occurs. The other modes do not change their L^2 nature. The attenuation constant α curves are reported in Fig. 17 (b): for almost all the modes which transform from L^2 to L^1 the attenuation constant decreases, as well as for the transition of the G_{00} from leaky L^1 to guided. As an example, the L_9^1 attenuation constant changes from $\alpha = 6.7 \times 10^3$ dB/cm, for $\theta = 30°$, to $\alpha = 13$ dB/cm for $\theta = 70°$. The mode L_{10}^1 exhibits the lowest attenuation constant $\alpha \leq 6$ dB/cm for $70° < \theta < 90°$. Some of the attenuation constant curves corresponding to the modes depicted in Fig. 17 (a) are not reported in Fig. 17 (b) in order to enhance figure readability. However these curves have a shape that is almost parallel to the L_{27}^2 curve, representing loss values which are intermediate between those of the L_{28}^2 and L_6^1 modes. As for the other dielectric tensor configurations, there are particular c axis orientations for which the electromagnetic field wavefunction profile can have intermediate guided-leaky characteristics. As an example, the typical leaky oscillations can be accompanied by a decreasing bounded (guided) shape. It can occur when there is a single guided eigenvalue while the other is leaky: the wavefunction profiles for the L_4^1 mode, having the refractive effective index $n_r = 2.26075$ for $\theta = 60°$ are shown in Fig. 18.

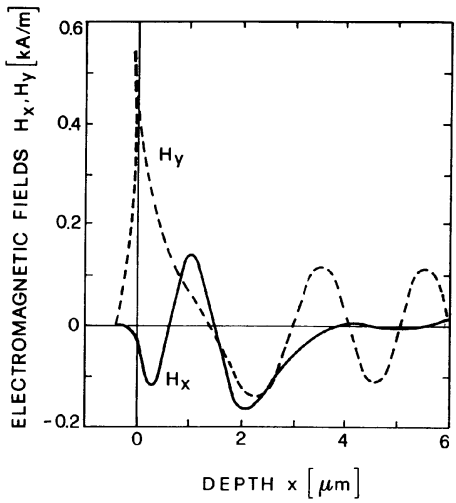

Figure 18. Mapping of the field component H_x, H_y for the L_4^1 leaky mode of the H:$LiNbO_3$ waveguide and $\theta = 60°$.

Thus, also for the PE waveguide, there are new transition angles from guided to leaky, when the optical c-axis is oriented near the x axis. In fact, if we suppose a rotation of the optical c-axis from the xz plane to the xy one, the modes $G_2, G_3, G_4, G_5, G_6, G_7, G_8$, which are guided for $\gamma \cong 90°$ in the equatorial dielectric tensor configuration, quickly transform into L^1 waves when the dielectric tensor assumes a longitudinal configuration.

5. APPLICATION AND CONCLUSION

Multimode $LiNbO_3$ waveguides permit a larger class of four-wave-mixing processes with respect to the non-linear phenomena observed for bulk crystals. This is due to the existence of different leaky and guided modes that may be parametrically coupled, and to the small waveguide thickness that favours recording of gratings. So a large variety of promising photorefractive effect applications becomes more feasible: information storage, real-time holographic recording, beam deflection, optical amplification, optical interconnections and neural networking [12].

Due to the richness of the supported modes, waveguiding structures similar to those considered in this work but iron diffused may be used in the generation and amplification of new guided or leaky waves using a single pump beam. In the past, experimental results demonstrated the possibility of obtaining independent holograms restored under different voltages, by using suitable electrodes [13]. The diffraction efficiency reaches its maximum if the same voltage used during the restoring is applied again during the readout. Nowadays, suitable thermal processes allow information storage to be fixed via recording phase volume holograms for virtually infinite time (10^5 years). Moreover, high density memories, with capacities of $0.5\,\mathrm{Gbits/cm^3}$, can be obtained by rotating the crystal by $0.1°$ after each optical grating recording. The possibility of modifying the Bragg condition by means of an external bias field allows suitable switches to be built. The diffraction process has a very strong angular selectivity that is basic in angular multiplexing. This aspect can be advantageously exploited in volume optical interconnection, to simulate the performance of the brain, in optical neural networks and associative memories.

The considered structures may have another interesting application in the fabrication of a high performance leaky waveguide modulator [14]. The use of leaky modes can be easily justified by considering

the optical rays theory. In fact, if the modulated mode is of a high-order then its representing ray makes a great number of passes travelling through the dielectric region that lies under the electrodes. So the distributed electrooptic effect of the material acts for an effective length that increases by increasing the modal order of the employed wave and the leaky modulator can have smaller geometrical parameters with respect to those of the same device based on guided propagation. Moreover, the modulator operation bandwidth becomes higher by decreasing its geometry. Transit time limitations can be exceeded via the travelling-wave configuration. Finally, thanks to the investigation developed in this paper, it is possible to choose a suitable waveguiding structure in order to refine the optical switching device proposed by Yamanouchi et. al. [8]. The switch was based on the conversion from leaky to guided modes for a rotated Y-cut Ti:$LiNbO_3$ waveguide. In particular the conversion was obtained electrooptically. In fact, the electric field applied between two electrodes induces a relative permittivity tensor component change which can be expressed in terms of the change Δb of the dielectric impermeability tensor b by means of the following relation [9]:

$$\Delta b_i = \sum_{j=1}^{3} r_{ij}^T E_j \quad (i = 1, 6)$$

where r^T is the third-rank electro-optic tensor at constant stress T and E is the applied electric field. Because the switching properties of the device depend critically on the beam angle, Yamanouchi et. al. controlled the conversion angle by applying a proper dc bias electric field. The modal transition causes a strong change of the decay constant. The exact theoretical analysis requires the calculation of the permittivity component change and the eigenvalue equation solution, for different applied electric fields, near the chosen transition angle. The refractive effective indices and the corresponding attenuation constants may be very accurately identified using our code. However, approximately but without making great errors, it must be concluded that the electrooptic effect causes a loss change similar to that induced by a slight rotation of the optical c-axis near the transition angle. In fact, in both cases the modal transition occurs. Moreover, the best waveguiding structure, such as the suitable metal electrodes, and the best optical c-axis orientations can be chosen by observing

the loss plots versus the axis direction reported in this work. In particular, for the switch refinement, the Ti:LiNbO$_3$ waveguides having an equatorial dielectric tensor configuration can be excluded because of their slighter attenuation constant variation. This is true also for the Ti:LiNbO$_3$ waveguides having a longitudinal dielectric tensor configuration [10]. On the contrary, for the Ti:LiNbO$_3$ waveguide having polar dielectric tensor configuration [4], suitable transition angles, for which there are stronger attenuation constant variations, exist. However, the H:LiNbO$_3$ technology allows waveguides to be made which exhibit more appropriate attenuation constant behaviour. In particular, the more suitable dielectric tensor configurations are the equatorial and the polar ones, while the longitudinal must be excluded. For example, in the polar case, both the G_{00} and the L^1_{10} modes exhibit very strong changes of the loss values near their conversion angle: about 135 [dB/cm]/ $^\circ$ and 295 [dB/cm]/ $^\circ$ when they transform into L^1 and L^2 for $\theta \cong 55^\circ$ and $\theta \cong 50^\circ$, respectively. We conclude that a refined switch may advantageously base its operation principle on the modal conversion from L^1 to L^2 mode. To minimize the loss propagation when the switch is "on" the attenuation constant must be the smallest, so Ag electrodes should be utilized. This choice can be explained by observing the G_0 attenuation constant diagram for the different metal layer, Ni, Al, Ag, Au, in the equatorial dielectric tensor configuration, as reported in Fig. 8b and Figs. 10–12b. This conclusion agrees with the results previously obtained for the polar dielectric tensor configuration [4] even if the Al technology is more suitable to make metal electrodes.

ACKNOWLEDGEMENTS

The authors want to thank Mr. Antonio Crudele for typing and graphic support. This work has been written with the financial support of MURST 40% 1995.

REFERENCES

1. De Sario, M., M. N. Armenise, C. Canali, P. Franzoni, J. Singh, R. H. Hutchins, and R. M. De La Rue, "In-plane scattering in titanium diffused LiNbO$_3$ optical waveguide," *Applied Physics Letters*, Vol. 45, 326–329, 1984.

2. Helmfrid, S., F. Laurell and G. Arvidsson, "Optical parametric amplification of a 1.54 μm single mode DFB laser in a Ti:$LiNbO_3$ waveguide," *IEEE Journal of Lightwave Technology*, Vol. 11, No. 9, 1459–1469, 1993.
3. Becker, P., R. Brinkmann, H. Suche, and W. Sohler, "Er-diffused Ti:$LiNbO_3$ waveguide laser emitting at 1563 and 1576 nm wavelength," *Integrated Photonics Research*, Technical Digest Series, Vol. 10, 314–315, 1992.
4. De Sario, M., A. D'Orazio, V. Petruzzelli, and F. Prudenzano, "Leaky mode propagation in planar multilayers inhomogeneous birefringent waveguides: polar dielectric tensor configuration," *Journal of Physics D: Applied Physics*, Vol. 25, No. 8, 1172–1181, 1992.
5. Webjorn, J., "Structural influence of proton exchange on domain inverted lithium niobate revealed by means of selective etching," *IEEE Journal of Lightwave Technology*, Vol. 11, No. 4, 589–594, 1993.
6. Hinkov, I., and V. Hinkov, "Acoustooptic collinear TE-TM mode conversion in a two layer Ti-indiffused and proton-exchanged waveguide structure in $LiNbO_3$," *Optical and Quantum Electronics*, Vol. 25, No. 11, 195–200, 1993.
7. Novikov, A. D., S. G. Odoulov, V. M. Shandarov, E. S. Shandarov, and S. M. Shandarov, "Parametric intermode scattering in planar $LiNbO_3$ waveguides," *Journal of Optical Society of America B*, Vol. 8, No. 6, 1298–1303, 1991.
8. Yamanouchi, K., M. Yasumoto, and K. Shibayama, "Optical switching device using leaky surface waves," *IEEE Journal of Quantum Electronics*, Vol. QE, No. 11, 863–865, 1978.
9. d'Alessandro, A., A. D'Orazio, M. De Sario, V. Petruzzelli, and F. Prudenzano, "Refined modeling of traveling-wave Ti:$LiNbO_3$ channel waveguide modulator," *Fiber and Integrated Optics*, Vol. 10, 141–157, 1993.
10. D'Orazio, A., M. De Sario, V. Petruzzelli, and F. Prudenzano, "Leaky mode propagation in planar multilayer birefringent waveguides: longitudinal dielectric tensor configuration," *IEEE J. of Lightwave Technology*, Vol. 12, No. 3, 1172–1181,1994.
11. Armenise, M. N., C. Canali, M. De Sario, and E. Zanoni, "Fabrication and characteristics of optical waveguides on $LiNbO_3$," *Materials Chemistry and Physics*, Vol. 9, Paper MAC81, Elsevier Sequoia S.A., 267–284, 1983.
12. Agullò-Lòpez, F., J. M. Cabrera and F. Agullò-Rueda, *Electrooptics phenomena, materials and applications*, Academic Press, London, 1994.

13. Petrov, M. P., S. l. Stepanov, and A. A. Kamshilin, "Image polarisation characteristics storage in birefringent crystal," *Optics Communications*, Vol. 21, No. 2, 297–300, 1977.
14. Desmulliez, M. P. Y., B. S. Ryvkin, A. C. Walker, and B. S. Wherrett, "Leaky-waveguide modulator using distributed coupling of light," *Optics Communications*, Vol. 110, 60–66,1994.